Buried three dimensional magnetisation structures and singularities revealed with X-ray vector nanotomography

Claire Donnelly*[1,2], Manuel Guizar-Sicairos*[2], Valerio Scagnoli[1,2], Sebastian Gliga*[3], Mirko Holler[2], Jörg Raabe[2], Laura J. Heyderman[1,2].

[1] Laboratory for Mesoscopic Systems, Department of Materials, ETH Zurich, 8093 Zurich, Switzerland.

[2] Paul Scherrer Institute, 5232 Villigen PSI, Switzerland.

[3] School of Physics and Astronomy, University of Glasgow, Glasgow, G12 8QQ, United Kingdom.

In soft ferromagnetic materials, the smoothly varying magnetisation leads to the formation of fundamental patterns such as domains, vortices or domain walls [1]. Over the past decades, these have been studied extensively in thin films where the magnetisation is accessible with current imaging methods. In thick samples, however, where the magnetisation is intrinsically three dimensional, the direct determination of the rich and complex magnetic structure still represents a challenge [1-3]. We have developed hard X-ray magnetic tomography with which one can determine the three dimensional magnetic configuration at the nanoscale within micrometre-sized samples. We image the structure of the magnetisation within a soft magnetic pillar of diameter 5 μm with a spatial resolution of 100 nm and, within the bulk, we observe a complex magnetic configuration that consists of vortices and antivortices that form cross-tie and vortex walls along orthogonal planes. At the intersections of these structures, magnetic singularities are present - so-called Bloch points - which were predicted by Feldtkeller over fifty years ago [4] but have so far not been directly measured. Here we determine the three dimensional magnetic structure in the immediate vicinity of the Bloch points, that until now has only been accessible through micromagnetic simulations, and identify two possible energetically favourable magnetisation configurations: a circulating magnetisation structure [5] and a twisted state that corresponds to an anti-Bloch point. Our imaging method opens new possibilities for the fundamental study of topological magnetic structures in bulk systems [6]. This knowledge of the internal nanomagnetic textures is critical for understanding macroscopic magnetic properties and designing new bulk magnets for applications [7].

Until now, magnetic investigations at the nanoscale have only been possible in transmission with soft X-ray [8] and electron [9-12] microscopy, which are ideally suited to probe surface and thin film magnetism. These investigations have recently been extended towards three dimensional patterned [9, 13], rolled or curved structures [8] by adapting existing microscopy

techniques to tomographic imaging [8-12]. The introduction of three dimensionality provides additional degrees of freedom, and can result in novel properties [14, 15] such as magnetochirality [15] and induced anisotropies [14], but the imaging is nevertheless limited to thin film investigations. New approaches are required in order to image the three-dimensional structure of extended and bulk magnetic systems, for example, in order to elucidate the nature of observed surface domain patterns, such as in iron whiskers [16]. From the point of view of applications, the performance of soft magnets with high permeability, essential for inductive applications such as data storage, motors or sensors [1, 7, 8], as well as that of permanent magnets, used for energy harvesting, mechanical and sensor applications [7], is determined by the magnetic microstructure. In this context, an important yet elusive micromagnetic structure is the Bloch point, a singularity in the magnetisation which has been predicted to be decisive both for determining the topology of the magnetisation [4] and in shaping magnetic behaviour such as pinning to the atomic lattice [17] and vortex dynamics [18-20].

In terms of the three dimensional imaging of extended systems, first investigations have been achieved with neutron tomographic imaging techniques [21, 22] reaching spatial resolutions of 10-100 μm, while sub-micrometre resolution has only been obtained with a material-destructive technique [3]. In contrast, hard X-rays offer a combination of high spatial resolution and high penetration depth, and thus provide a flexible solution to tomographic imaging. With recent progress in high spatial resolution hard X-ray investigations of micrometre-sized magnetic systems [23] and hard X-ray tomography of the electron density of micrometre-sized samples having reached 16 nm [24], the combination of high spatial resolution and high penetration of hard X-rays therefore provides a promising means for high resolution three dimensional studies of ferromagnetic systems [14].

One of the key challenges of three-dimensional magnetic investigations concerns the development of an appropriate tomographic algorithm to recover the three-dimensional magnetic vector field. In contrast to traditional tomography, where one retrieves a scalar value such as the electron density at each point, for magnetic tomography one needs to reconstruct three separate components of the magnetisation for each individual voxel. So far this has been achieved in specific samples by implementing available constraints, for example with electron tomography by reducing the complexity through Maxwell's equations [12, 25]. For soft X-rays, the magnetic vector field has been obtained by incorporating prior knowledge of the magnetic properties of the material [8]. Here we combine a new dual-axis measurement strategy with a tomographic reconstruction algorithm to obtain an *ab-initio*

retrieval of the magnetisation vector field with nanoscale resolution, exploiting the high penetration depth of hard X-rays to image a sample with a diameter of several micrometres.

Using hard X-ray magnetic tomography, we determine the three-dimensional magnetisation configuration of a soft $GdCo_2$ magnetic cylinder [26] of diameter 5 µm. The two magnetic sublattices of the ferrimagnet are strongly coupled antiparallel to each other leading to an effective soft ferromagnetic behaviour [27]. The investigated sample (Figure 1a insets) was cut from a nugget using focused ion beam milling and mounted on top of a tomography pin using a micromanipulator. By measuring at the absorption edge of the magnetic material with circularly polarised X-rays, one can exploit X-ray magnetic circular dichroism (XMCD) that is sensitive to the component of the magnetisation parallel to the X-ray beam [28]. A 2D XMCD projection of the pillar (Figure 1c), already gives an indication that the internal magnetic structure is complex. We now perform magnetic vector tomography to elucidate the details of the three dimensional internal structure at the nanoscale.

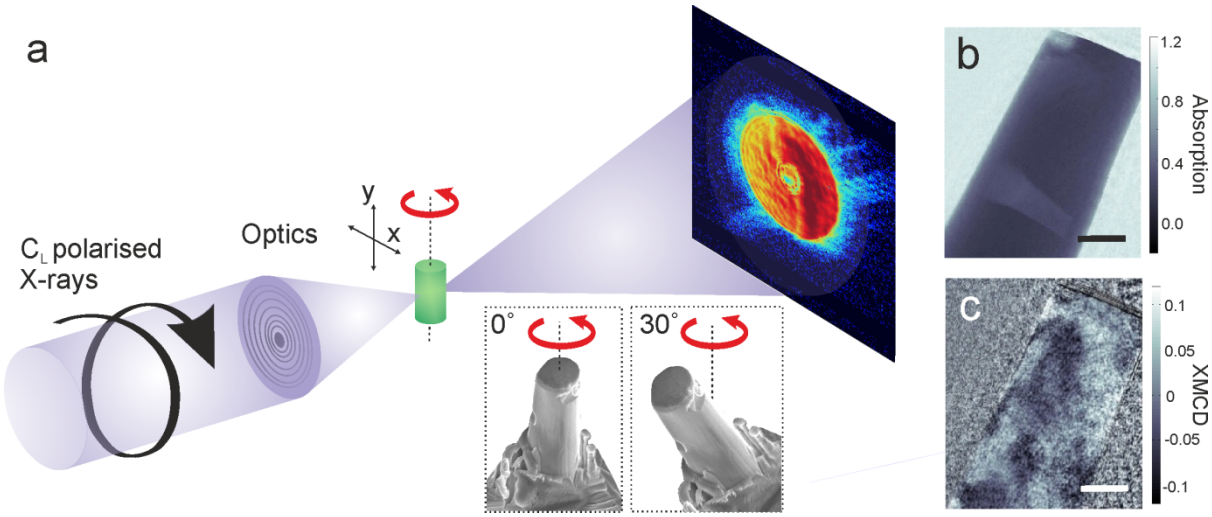

Figure 1 X-ray magnetic tomography. (a) Schematic of setup with circularly polarised X-rays incident on the sample. Ptychographic scans are performed where the diffraction pattern is measured in the far field at a number of sample positions in the x-y plane with mutually overlapping illumination. To have access to all three components of the magnetisation, tomographic data is collected for two axes of rotation (see insets). (b) A ptychographic reconstruction of the absorption measured with a single circular polarisation contains both electronic and magnetic contrast. (c) A purely magnetic image can be obtained by taking the difference between images recorded with left and right circularly polarised light and is shown in terms of the difference in absorption across the absorption edge (see Materials and Methods section) [23]. Scale bars in (b) and (c) represent 2 µm.

Experimentally, magnetic tomography is performed as shown in Figure 1a to determine the as-grown magnetisation state of the sample. For each axis of rotation, two-dimensional absorption images are recorded using circular left polarised X-rays [29] with hard X-ray dichroic ptychography [23] for 512 different orientations distributed over 360° with equal angular spacing. The details of the tomographic reconstruction and calculations of the spatial resolution are described in the Materials and Methods section “Tomographic

Reconstructions". An estimate for the spatial resolution was obtained via Fourier shell correlation (FSC) [30] of the absolute values of the in-plane magnetisation using the half-bit threshold criteria. The spatial resolution was found to range between 97 nm and 127 nm, depending on the direction or plane considered. The direction dependence of the spatial resolution results from the m_y component receiving effectively less flux due to the geometry of the experiment. This estimate was confirmed by the fact that we can resolve a magnetic vortex from an antivortex in the x-z plane with a separation of 126 nm (See Materials and Methods section "Spatial Resolution").

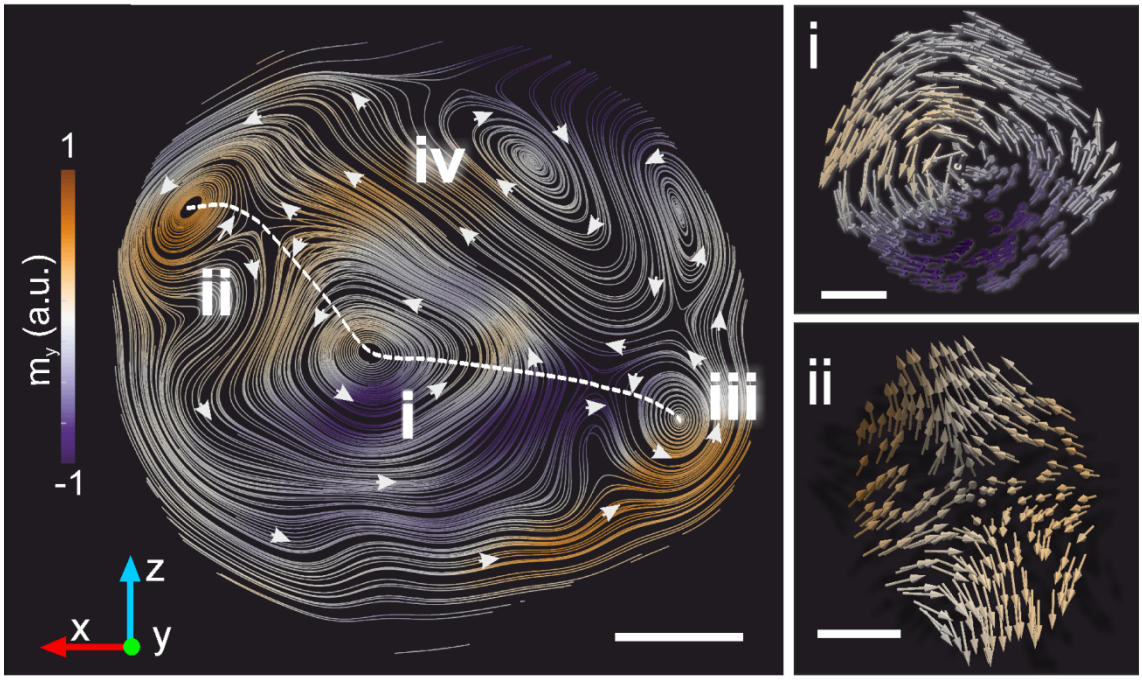

Figure 2: Axial tomographic slice. A section taken perpendicular to the long axis of the cylindrical sample is shown where the streamlines represent the x-z components of the magnetisation. Different magnetic structures can be identified: Anti-clockwise vortices (i and iii), a clockwise vortex (iv) and an antivortex (ii) between two vortices with the same vorticity (i and iii). The 3D magnetic nanostructure of the vortex (i) and the antivortex (ii) is shown in more detail in the insets to the right of the figure. A section of a cross-tie wall containing a succession of vortex and antivortex structures is indicated by the dashed white line. Scale bars represent 1 μm (main image) and 300 nm (right hand insets).

To understand the complex magnetic configuration, we first consider axial slices of the pillar: a 40 nm-thick slice is presented in the left panel of Figure 2 with the direction of the magnetisation in the x-z plane represented using streamlines whose colour indicates the y-component of the magnetisation (along the long axis of the pillar). In contrast to thin films, the magnetic structures in the bulk are not confined to a single plane. They display a non-zero magnetisation component along the axis of the pillar (m_y), which is not limited to the vicinity of the cores of the structures, as is the case in thin films. The magnetic configuration consists of a dense arrangement of magnetic vortices with both negative and positive vorticities (corresponding to the clockwise and anticlockwise curling of the magnetisation).

The structure of an anticlockwise vortex (i) is shown in detail in the top right panel of Figure 2. Between vortices with opposite vorticity (i and iv, for example) the magnetisation is almost uniform, whereas between vortices with identical vorticities (such as i and iii), the magnetisation is inhomogeneous, giving rise to a cross-tie wall traversing the pillar (a section of which is indicated by the dashed line) containing a succession of vortex and antivortex structures (such as ii) whose detailed magnetic configuration can be seen in the bottom right panel of Figure 2.

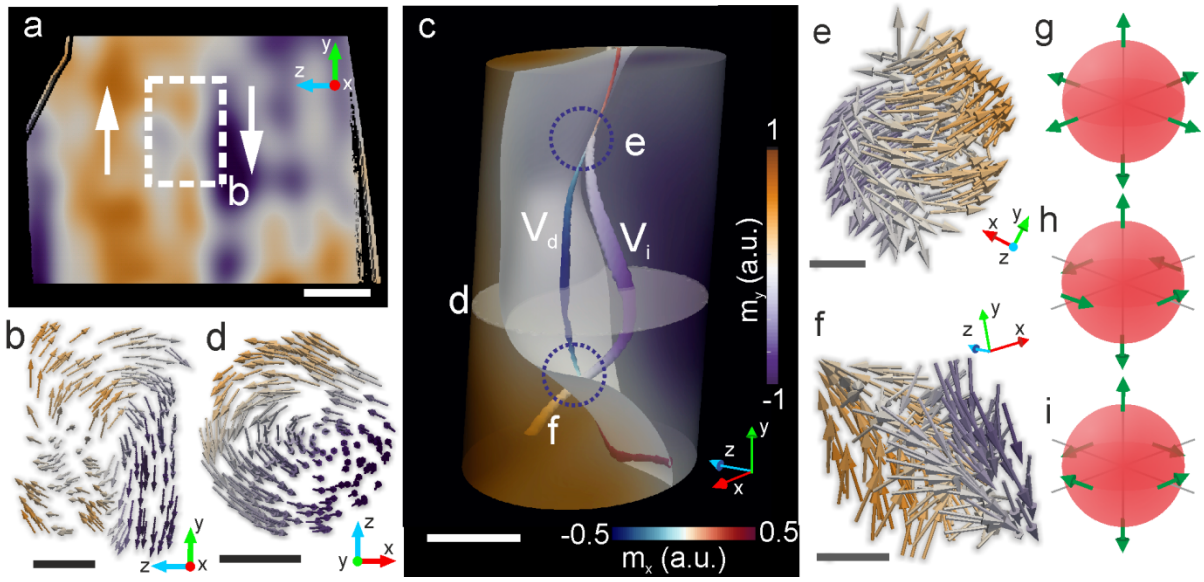

Figure 3 Detailed 3D magnetic domain configuration surrounding vortex (i). (a) Y-component of the magnetisation in a vertical slice through the pillar. Two main large domains of negative (purple) and positive (orange) m_y are indicated. (b) The magnetic configuration of a vortex structure in the vicinity of the domain wall indicated by a dashed rectangle in (a). (c) The domain wall is shown as a white $m_y = 0$ isosurface within a portion of the pillar, in addition to the core of the vortex wall ($V_{d,}$, coloured by the direction of the magnetisation of the core, aligned along $\hat{x}$) which runs along the domain wall. The magnetic configuration of an axial slice through the portion of the pillar, indicated by the white disk, in is given in (d). The core of vortex (i) in Figure 2, V_i, extends through the length of the pillar and is mapped by an isosurface whose colour represents the magnetisation orientation (orange and purple for $+m_y$ and $-m_y$, respectively). The vortex core crosses the domain wall at its core at a number of points: two examples (e) and (f) are circled. At these points $m_x = m_y = m_z = 0$, corresponding to the presence of a magnetic singularity, or Bloch point. While the Bloch points cannot be resolved, the magnetisation configuration in their vicinity (within a 125 nm radius) is shown in (e) and (f). For reference, three possible configurations for the Bloch point are shown schematically: (g) a hedgehog, or diverging Bloch Point, (h) a circulating Bloch point, and (i) a contra-circulating Bloch point, where the vortex in (h) is replaced by an antivortex. Scale bars represent (a) 1 μm, (b-d) 500 nm and (e-f) 100 nm.

Considering the full three dimensional magnetisation surrounding vortex (i) in Figure 2, which extends through the height of the pillar, we observe a complex structure due to the large number of degrees of freedom resulting from the lack of spatial confinement or anisotropy. The reconstruction reveals two large domains of positive and negative m_y (Figure 3a), separated by a domain wall extending along the height of the pillar. This domain wall is a vortex wall as shown in Figure 3b. In contrast to domain walls in thin films and in high anisotropy materials, which typically extend over a few to tens of nanometres, here the

domain wall extends over a few hundred nanometres as expected in an ideal soft ferromagnet [31] in the absence of lateral confinement. The magnetic configuration also contains a number of inhomogeneous structures, which are magnetostatically favoured despite the additional exchange energy required. The central plane of the domain wall is mapped using the $m_y = 0$ (white) isosurface for a subsection of the pillar in Figure 3c with the core of the vortex of the domain wall (V_d), coloured by its polarisation, running along the domain wall in Figure 3c (the detailed correspondence between Figure 2 and Figure 3a and c is given in Extended Data S6). The vortex, V_i (see vortex i in Figure 2) intersects this domain wall at multiple locations, coinciding with the core of the vortex domain wall, V_d. At these intersections the polarisation, *i.e.* the orientation of the magnetisation within the core of both vortices, reverses. This reversal can be seen in Figure 3c at point f where the colour indicates the direction of the core of the vortex V_i, which changes from $+m_y$ (orange) to $-m_y$ (purple) on either side of the wall. The polarisation of the domain wall vortex V_d also reverses from $+m_x$ (red) to $-m_x$ (blue).

At the points of intersection of the vortex core V_i with the domain wall (indicated by circles (e) and (f) in Figure 3c), $m_x = m_y = m_z = 0$, corresponding to a magnetic singularity, or Bloch point. While such singularities were predicted analytically by Feldtkeller [4] and have been studied theoretically, they have so far not been directly observed experimentally. The Bloch point contains a singularity around which the magnetic order is destroyed at a radius of the order of a few lattice constants [17]. The structure of the Bloch point is determined by the magnetisation surrounding the singularity on a radius of the order of the exchange length. Here we resolve the three dimensional magnetisation configuration in the vicinity of a pair of singularities, with a spatial resolution of 100 nm, as shown in Figure 3e,f. The magnetisation distribution observed in Figure 3e is in agreement with the one predicted by micromagnetic simulations around a circulating Bloch point (schematically illustrated in Figure 3h) [5]. While the prototypical structure of a Bloch point is a “hedgehog”, with the magnetisation radially diverging around a central point (Figure 3g), the circulating Bloch point structure (Figure 3e) is more stable due to local magnetic flux closure [5] and the structure thus extends beyond the exchange length from the singularity. For other types of Bloch points, such as the one in Figure 3f, micromagnetic studies have shown that, beyond a radius equal to the exchange length of the material, the magnetisation becomes “twisted” in order to achieve a magnetostatically stable configuration that effectively screens the monopole created by the singularity (see also Extended Data S3). Considering that, within the bulk, Bloch points can only be created in pairs, we expect this structure to correspond to an “anti-Bloch point” (illustrated in Figure 3i). Such observations constitute a basis for elucidating the relationship between the structure of the magnetisation around the Bloch point on the nm scale and the

complex surrounding magnetic configuration, which spans a sphere tens of nm in radius, opening for the first time a possibility for their experimental study.

In this first demonstration of hard X-ray magnetic tomography, we employ dichroic ptychography as an imaging technique that is applicable to a wide variety of materials and sample geometries. Given that we make use of the absorption part of the transmission function, this magnetic tomography technique can in principle be combined with any high resolution X-ray microscopy technique such as full field [32] or cone beam propagation microscopy [33, 34], and we envision that this technique can be implemented at a number of current and future synchrotrons. With advances in X-ray optics and the advent of upgraded and fourth generation synchrotrons, the coherent flux available can be expected to increase by 2-3 orders of magnitude in the near future [35, 36], bringing hard X-ray magnetic tomography down to a spatial resolution of the order of 20 nm.

Material and Methods

Magnetic tomography

The development of the magnetic tomographic algorithm relies on the precise understanding of the angular dependence of the magnetic signal. For the case of X-ray magnetic tomography, we exploit X-ray magnetic circular dichroism, for which the XMCD signal takes a maximum positive (negative) value when the magnetic moment is parallel (antiparallel) to the X-ray propagation direction and is zero when it is perpendicular. Upon 180° rotation of the sample, the XMCD signal is therefore reversed in sign, and we use this fact to separate the electronic from magnetic contribution in our tomography reconstruction by acquiring data over a 360° angular range, in contrast to the usual 180° range used for conventional tomography. A single measurement, also referred to as a projection, gives the integral of the magnetisation component parallel to the X-ray beam, which means that a dataset measured around a single rotation axis ($\hat{y}$) perpendicular to the X-ray direction only probes the magnetisation in the plane perpendicular to the axis of rotation (m_x, m_z), and not the component of the magnetisation parallel to the axis of rotation (m_y). In order to access all three components of the magnetisation, we therefore perform dual-axis tomography, where we record data with the sample at 0° and 30° with respect to the rotation axis (see insets of Figure 1a). In this manner we record a full dataset with access to all three spatial components of the magnetisation.

Experimental methods

Magnetic tomography was performed at the cSAXS beamline at the Swiss Light Source, Paul Scherrer Institut, Switzerland, using a high resolution interferometrically controlled tomography setup [24]. As found in a previous work, the maximal contrast and signal to noise ratio is available with the absorption part of the complex XMCD signal [23] and, in particular, the XMCD signal at the Gd L_3 edge is the strongest signal available in the hard X-ray regime. Therefore, dual axis magnetic tomography was performed with circularly left polarised light at the Gd L_3 edge with a photon energy of 7.246 keV chosen to maximise the absorption XMCD signal. The 2D absorption images were measured with X-ray ptychography [37-39], a coherent diffractive imaging technique that offers access to the full complex transmission function of the sample with high spatial resolution. In particular, by combining X-ray ptychography with resonant X-rays with a single circular polarisation, each image contains both magnetic and electronic contrast [23].

Circularly polarised X-rays were produced as in [23] by converting horizontally polarised X-rays emitted from the undulator source using a 500 μm-thick diamond quarter-wave plate [40]. The degree of polarization of the X-rays was determined using a polarization analyser setup [29] and was found to be over 99%, with the phase plate absorbing approximately 65% of the incident light.

For X-ray ptychography we define an X-ray illumination of 4 μm on the sample with a combination of a central stop of diameter 40 μm, order sorting aperture of diameter 30 μm, and a Fresnel zone plate with diameter 150 μm and an outermost zone width of 60 nm. To achieve an illumination of 4 μm, the sample was placed 1.18 mm downstream of the focus of the Fresnel zone plate. The total flux incident on the sample is approximately 3×10^8 photons/s. Ptychography scans were performed on a grid of concentric circles [41] with a radial separation of 0.4 μm and with a field of view of 8 μm × 7 μm (351 scanning points) and 13 μm × 9 μm (730 scanning points) for the 0° (not tilted) and 30° tilt angles of the sample, respectively. At each of the scanning points, a diffraction pattern was recorded with an exposure time of 0.2 s on a Pilatus detector [42, 43] placed 7.243 m downstream of the sample.

Ptychographic reconstructions were performed using 500 iterations of the difference-map algorithm [38] followed by 200 iterations of maximum likelihood refinement [44, 45] using 400×400 pixels of the detector, resulting in projections that had a pixel size of 18 nm. An initial guess for the illumination was obtained through a previous ptychography measurement on a strongly scattering test object and, during the reconstruction, both the object and the illumination were iteratively optimised.

The photon energy was calibrated by performing spectroscopic ptychography across the Gd L_3 edge in order to obtain an absorption spectrum that could be compared with reference data [46]. In this way, the energy at which the XMCD signal is maximal was determined. Ptychography scans of the $GdCo_2$ pillar were performed for energies ranging between 7.2025 keV and 7.2815 keV in steps of 1.5 eV as described in [23]. The reconstructions were aligned to within a small fraction of a pixel [47] and the absorption part of each complex reconstruction was normalised using a region of air whose transmission should be equal to one. An absorption spectrum was obtained by averaging a section of the image containing material and plotting these values as a function of energy (see Extended Data S1.). The absorption spectrum was then compared to reference spectra measured on a similar material [46] to determine the energy corresponding to the maximum XMCD signal. The difference in absorption across the absorption edge, Δ_{edge} is indicated in Extended Data S1. As in [23], we define the XMCD signal in terms of Δ_{edge} , which on-resonance equates to approximately 10%. For the tomogram of the non-tilted sample, 512 projections were measured with equal angular spacing over 360°. In order to account for the gaps between detector modules, where we lose part of the diffraction pattern, neighbouring projections were measured for different detector positions [24] and reconstructed together in pairs of scans that share a common illumination function [48]. Then the entire sample pin was remounted in the setup at a tilt angle of 30° using a dedicated sample holder and a tomogram with the same tomographic angular resolution measured. Each individual image had a measurement time of 120 s and 246s for the 0° and 30° tilt angles, respectively, giving a total time of 52 hours for an investigated region of 351 μm^3. The radiation dose applied to the sample during the measurement was 2.8×10^9 Gy.

As a validation for the tomographic reconstruction, 2D XMCD images were measured as described in [23]. The images were taken at a photon energy of 7.246 keV with the sample in the tilted geometry rotating the sample in 30° steps from 0° to 150°. The ptychographic scan parameters were the same as those used for the tomogram. For each angle, 10 images for each circular polarisation (left and right) were aligned [47] and averaged, with each averaged XMCD image requiring a total measurement time of 1h 40 min. The 2D XMCD images are compared with equivalent projections computed from the reconstructed magnetic tomogram in Extended Data S2 and show very good agreement.

Tomographic reconstructions:

Non-magnetic tomographic reconstruction

For each dataset at 0° and 30°, the following postprocessing routine was performed. To obtain an optimal tomographic reconstruction, the set of projections are first preprocessed and aligned to high precision. As a first step, regions of air around the pillar are selected which serve as references in order to normalise the overall transmission, and remove linear and constant offsets to the phase part of the transmissivity [49]. The phase information, which has higher signal-to-noise ratio than the absorption part, is then used to refine the alignment of the projections following the procedure in [49] and, as a final step, the horizontal alignment is refined based on tomographic consistency [50]. These alignment values are subsequently applied to the complex-valued projections and an electron density tomogram is then obtained from the phase of the projections by applying a modified filtered back projection that is insensitive to phase wrapping [49]. For the latter, the full range of sample rotation from 0° to 360° can be used because the magnetic contribution cancels for angles θ and $\theta + 180°$.

Magnetic tomographic reconstruction

The scattering factor of a material with a magnetic moment $\boldsymbol{m}(\boldsymbol{r})$ is dependent on both the electronic and magnetic scattering. For the case of circularly polarised light incident on a ferromagnetic sample in the limit of resonant small angle scattering [51], the scattering factor can be approximated to:

$$f = f_c \pm i f_m \hat{\boldsymbol{z}} \cdot \boldsymbol{m}(\boldsymbol{r})$$

where f_c is the electronic scattering factor, f_m is the magnetic scattering factor, $\boldsymbol{r} = (x, y, z)$ is the Cartesian coordinate vector, and $\hat{\boldsymbol{z}}$ is the direction of propagation of the X-rays. The magnetic signal that we measure with X-ray magnetic circular dichroism is therefore proportional to the component of the magnetisation parallel to the X-ray beam, and around one rotation axis, $\hat{y}$, the measurement is thereby only sensitive to the components of magnetisation in the x-z plane perpendicular to the axis of rotation, m_x and m_z. The projected signal as a function of tomographic angle for a single circular polarisation can be described as:

$$P_\theta(x, y) = \int \left[f_c(\boldsymbol{r}') + A\left(m_x(\boldsymbol{r}') \sin\theta + m_y(\boldsymbol{r}') \cos\theta \right) \right] dz$$

where $\boldsymbol{r}'$ is the Cartesian coordinate vector rotated by an angle θ, A is a constant that relates the XMCD signal to the magnetisation, and θ is the rotation angle of the sample with respect to the X-ray beam propagation direction.

A gradient-based iterative optimisation routine was used to retrieve $m_x(\boldsymbol{r})$ and $m_z(\boldsymbol{r})$ for each of the two tomographic measurements (at 0° and 30°), by minimising an error metric between projections of the reconstructed dataset with the measured projections.

The two electron density tomograms, obtained as detailed in Section *Non-magnetic tomographic reconstruction*, were registered to each other using Avizo software, which results in an affine transformation matrix relating the reconstructions of the pillar at 0° and 30° tilt to each other. The magnetic reconstructions are then combined using this affine transformation matrix by solving a system of linear simultaneous equations for each pixel to obtain the three dimensional magnetic vector field. As a last step, a 3D Hanning low-pass filter was used on each magnetic component to remove high–frequency noise. Paraview was used to visualise and map the magnetic configuration of the sample.

In the measurement we reconstruct a value of the XMCD signal on-resonance, which is proportional to the saturation magnetisation of the material. We normalise the components of the magnetisation to this value.

Spatial Resolution

The spatial resolution of the electron density tomograms was calculated as follows: the data were separated into two independent datasets with twice the angular spacing between tomographic projections. From these datasets, two independent tomograms were computed [24] and the spatial resolution estimated using Fourier Shell Correlation (FSC) with the half-bit criterion [30]. The spatial resolution was estimated to be 25 nm and 33 nm for the straight and tilted tomograms, respectively.

For the magnetisation vector field, two complimentary measurement techniques were employed:

1) Fourier Shell Correlation

We obtain an estimate for the spatial resolution by separating the datasets into two as above, and computing two 3D reconstructions of the magnetisation vector field. *We estimate the spatial resolution of each scalar magnetic component using FSC and find them to be 195 nm, 250 nm and 196 nm, for the m_x, m_y and m_z components, respectively.* Features in a vector field are often identified based on the amplitude or direction of the vector, which is a non-linear combination of the individual components. To estimate the spatial resolution of the vector field, we calculate the Fourier Shell correlation for the absolute value of the magnetisation in each of three perpendicular planes (See Extended Data S5), that is

$|\mathrm{m_{x,y}}| = \sqrt{\mathrm{m_x^2} + \mathrm{m_y^2}}$ for the x-y plane and similar for the x-z and the y-z planes, for which we find values of 125 nm, 97 nm and 127 nm, respectively.

The slightly different values of the spatial resolution corresponding to different directions, or planes, can be explained considering the geometry of the experimental setup: the $\mathrm{m_y}$ component is not probed in the first measurement series with the long axis of the pillar parallel to the rotation axis, and it is only probed in the tilted geometry in which the long axis of the pillar is at an angle of 30°. In contrast, the $\mathrm{m_x}$ and $\mathrm{m_z}$ components are probed in both geometries, and in total effectively receive 3.73× more flux. As the scattering signal is proportional to the 4th power of the smallest feature size [52], we expect the ratio of the spatial resolutions to be approximately $\sqrt[4]{3.73} = 1.39$, which results in an asymmetry in the spatial resolution that depends on the vector direction. We therefore estimate the spatial resolution of the magnetisation vector field to be between 97 nm and 127 nm, depending on the vector direction."

2) Resolution of nearby structures

Features of the magnetisation were identified using the absolute value of the magnitude of the magnetisation vector field. For a vortex, this is considered in the plane of the vortex $|m_{xz}| = \sqrt{{m_x}^2 + {m_z}^2}$. Towards the core of the vortex, the magnetisation slowly tilts out of the plane, meaning that the centre of the core of the vortex can be located by determining the local minimum of $|m_{xz}|$.

We consider the case of a vortex-antivortex pair separated by a decreasing distance as a function of height in figure S4 a-c, where the magnetisation is represented by streamlines. In Figure S4 d-f we show $|m_{xz}|$ for three consecutive axial slices, separated by 18 nm, where the centre of the core of the vortices and antivortices are seen as minima $|m_{xz}| = 0$. By considering both the direction (Fig S4b) and magnitude (Fig S4e) of the magnetisation, we estimate that we are able to resolve individual magnetic structures laterally separated by 126 nm (Fig. S4 b,e,h), in agreement with the FSC calculations.

Contributions:

J.R. and L.H. conceived the project. C.D., M.G.-S., V.S., M.H., and J.R. designed the experiment. M.H. and J.R. modified the instrument for the 30° tilt measurement. C.D., M.G.-S., V.S., M.H. and J.R. performed the experiment. C.D. and M.G.-S. developed the vector tomography reconstruction algorithm. C.D. performed the data analysis with support from

M.G-S and V.S.. C.D., S.G. and J.R. interpreted the magnetic results. C.D., M.G.-S. and S.G. wrote the manuscript with contributions from all authors.

Acknowledgements

X-ray measurements were performed at the cSAXS beamline at the Swiss Light Source, Paul Scherrer Institut, Switzerland. We thank Rose Marie Galera for providing the $GdCo_2$ nugget, and Stefan Stutz and Elisabeth Müller for the sample fabrication. SG was funded by the European Union's Horizon 2020 research and innovation programme under the Marie Sklodowska-Curie grant agreement No 708674.

Extended Data:

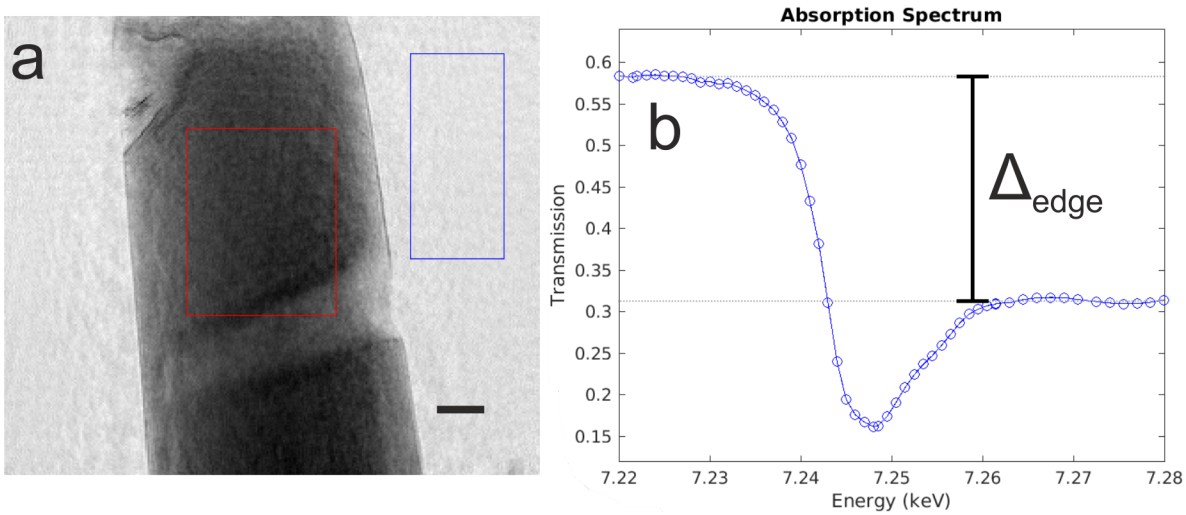

Figure S1 (a) Absorption part of a ptychographic reconstruction of the pillar measured at 7.2025 keV. Regions of air and material are highlighted by the blue and red boxes, respectively. Such images were measured for a range of energies between 7.2025 keV and 7.2815 keV in steps of 1.5 eV. (b) The transmission spectrum obtained from the range of images is shown, and the difference in absorption across the absorption edge, Δ_{edge}, is indicated.

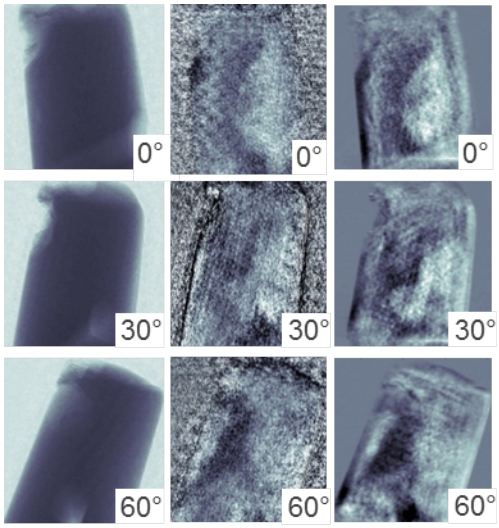

Figure S2: Validation of the magnetic reconstruction. Single polarisation images for different angles about the rotation axis (0°, 30° and 60°) are shown in the left hand column. In the central column, XMCD projections obtained by taking the difference between images measured with circular left and right polarisation are given, which are the integral of the magnetic component along the path of the X-ray beam. The equivalent projections obtained from the reconstructed

magnetic tomogram are given in the third column. Comparing the images in the central and right columns, the contrast and projection of the magnetisation match well. This good agreement validates the magnetic reconstruction.

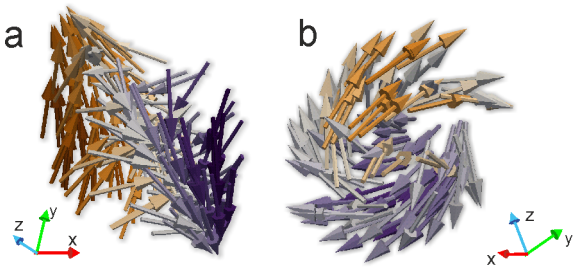

Figure S3: Structure of the magnetisation surrounding the singularity shown in Figure 3f. Different views are given, with respect to the plane of the domain wall, as shown in Figure 3c. (a) View parallel to the plane of the domain wall and (b) view perpendicular to the plane of the domain wall. The observed magnetic structure does not show a one-to-one correspondence to one of the Bloch point configurations in Figure 3g-i. While circulating Bloch points have been shown to minimise the magnetostatic energy due to their swirling magnetisation, this is not the case for other Bloch point configurations, where the magnetisation in the vicinity of the singularity is predicted to deform in order to minimise the magnetostatic energy. We therefore attribute the structure above to the redistribution of the magnetisation in order to screen the magnetostatic charge associated with the monopole generated by the diverging magnetisation at the Bloch point.

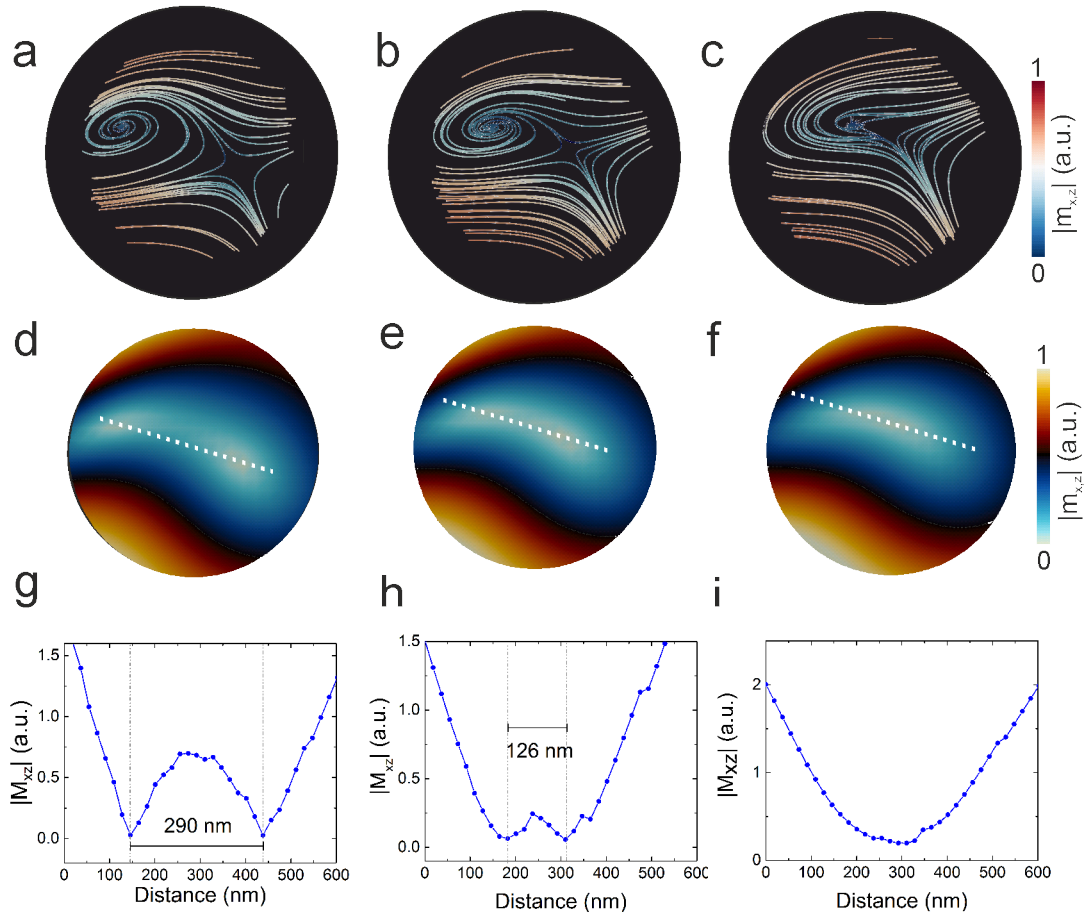

Figure S4: (a-c) streamlines indicating the direction of the magnetisation for three x-z slices at heights of 0 nm (mid-way through the pillar), +20 nm and +40 nm. A vortex–antivortex pair draw closer together as the height increases until they merge and can barely be resolved. (d-f) the absolute value of the magnetisation $|\boldsymbol{m_{xz}}| = \sqrt{\boldsymbol{m_x}^2 + \boldsymbol{m_z}^2}$ is shown for the same areas as a-c, where the cores of the vortex and antivortex are minima. (g-i) line profiles (indicated by the dotted line

in (d-f)) are taken through the images of $|\boldsymbol{m}_{xz}|$, where we show that we are able to resolve features in the vector field on the order of 126 nm (h) the structure of which can be seen clearly in (b), while in (i) the two structures can no longer be resolved.

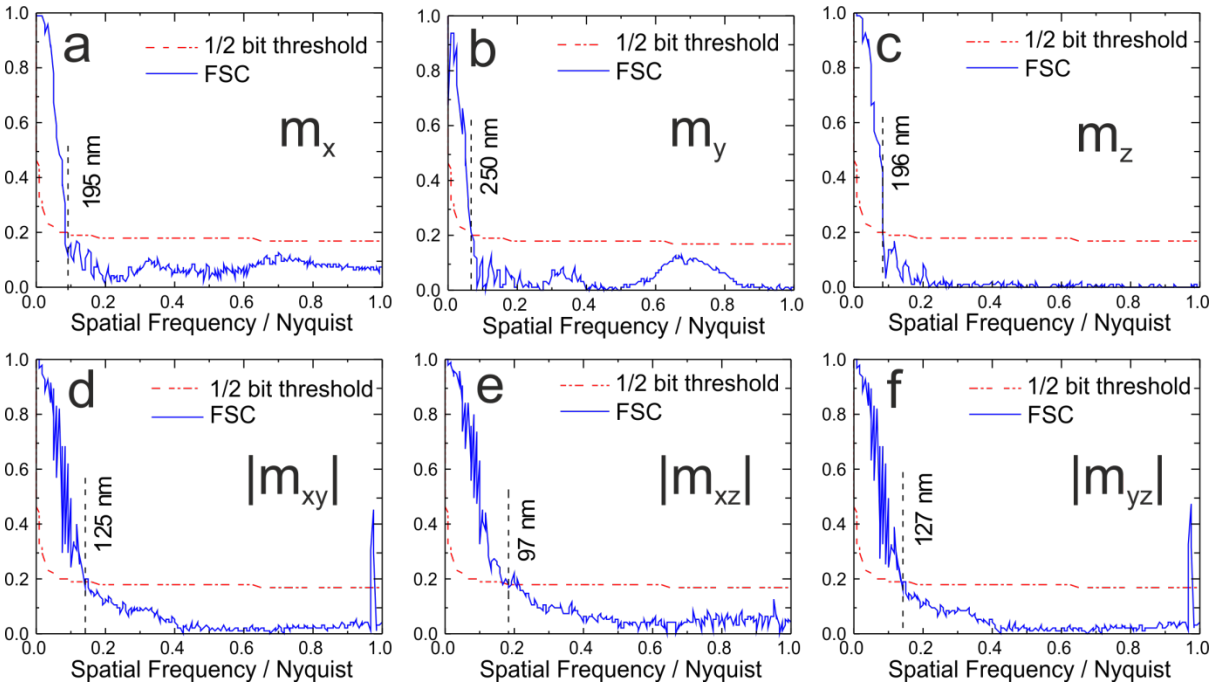

Figure S5: Estimation of the spatial resolution using Fourier shell correlation. Single components of the magnetisation vector: the spatial resolution of (a) $\boldsymbol{m}_x$ (b) $\boldsymbol{m}_y$ and (c) $\boldsymbol{m}_z$ are found to be 195 nm, 250 nm and 196 nm, respectively. The spatial resolution of $\boldsymbol{m}_y$ is lower because of lower sampling as explained in the text. To estimate the spatial resolution of the vector field, the Fourier shell correlations are calculated for $|\boldsymbol{m}_{xy}|$, $|\boldsymbol{m}_{xz}|$ and $|\boldsymbol{m}_{yz}|$ to be 125 nm, 97 nm and 127 nm, respectively. The xy and yz planes exhibit lower resolution due to the low sampling of $\boldsymbol{m}_y$.

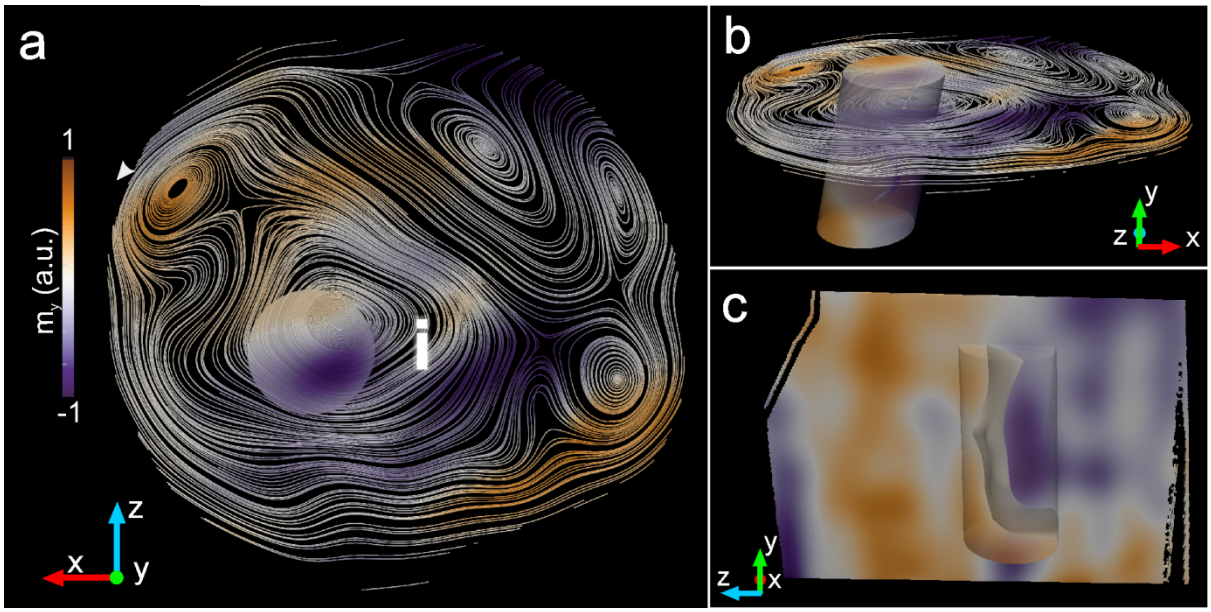

Figure S6: The correspondence of the 3D region in Figure 3c with the axial slice of Figure 2 (a) from above and (b) from the side. The core of the vortex (i) is mapped with an isosurface in (b). The relative positions of the slice in Figure 3a and the 3D region in Figure 3c are given in (c).

1. Hubert, A. and R. Schäfer, *Magnetic Domains: The Analysis of Magnetic Microstructures*. 1998: Springer.
2. Arrott, A.S., B. Heinrich, and A. Aharoni, *Point Singularities and Magnetization Reversal in Ideally Soft Ferromagnetic Cylinders.* Ieee Transactions on Magnetics, 1979. **15**(5): p. 1228-1235.
3. Shin, S., R. Schäfer, and B.C. De Cooman, *Three-dimensional Visualization of the Magnetic Microstructure in Bulk Fe-6.6 Pct Si.* Metallurgical and Materials Transactions A, 2013. **44**(9): p. 4239-4247.
4. Feldtkeller, E., *Mikromagnetisch Stetige und Unstetige Magnetisierungskonfigurationen.* Zeitschrift Fur Angewandte Physik, 1965. **19**(6): p. 530-+.
5. Elías, R.G. and A. Verga, *Magnetization structure of a Bloch point singularity.* The European Physical Journal B, 2011. **82**(2): p. 159.
6. Braun, H.-B., *Topological effects in nanomagnetism: from superparamagnetism to chiral quantum solitons.* Advances in Physics, 2012. **61**(1): p. 1-116.
7. Gutfleisch, O., et al., *Magnetic Materials and Devices for the 21st Century: Stronger, Lighter, and More Energy Efficient.* Advanced Materials, 2011. **23**(7): p. 821-842.
8. Streubel, R., et al., *Retrieving spin textures on curved magnetic thin films with full-field soft X-ray microscopies.* Nat Commun, 2015. **6**.
9. Phatak, C., et al., *Visualization of the Magnetic Structure of Sculpted Three-Dimensional Cobalt Nanospirals.* Nano Letters, 2014. **14**(2): p. 759-764.
10. Tanigaki, T., et al., *Three-Dimensional Observation of Magnetic Vortex Cores in Stacked Ferromagnetic Discs.* Nano Letters, 2015. **15**(2): p. 1309-1314.
11. Junginger, F., et al., *Quantitative determination of vortex core dimensions in head-to-head domain walls using off-axis electron holography.* Applied Physics Letters, 2008. **92**(11): p. 112502.
12. Phatak, C., A.K. Petford-Long, and M. De Graef, *Three-Dimensional Study of the Vector Potential of Magnetic Structures.* Physical Review Letters, 2010. **104**(25): p. 253901.
13. Donnelly, C., et al., *Element-Specific X-Ray Phase Tomography of 3D Structures at the Nanoscale.* Physical Review Letters, 2015. **114**(11): p. 115501.
14. Streubel, R., et al., *Magnetism in curved geometries.* Journal of Physics D: Applied Physics, 2016. **49**(36): p. 363001.
15. Hertel, R., *Curvature-induced magnetochirality.* Spin, 2013. **3**(3): p. 1340009 (9 pp.)-1340009 (9 pp.).
16. Arrott, A.S., *Visualization and Interpretation of Magnetic Configurations Using Magnetic Charge.* IEEE Magnetics Letters, 2016. **7**: p. 1-5.
17. Andreas, C., A. Kákay, and R. Hertel, *Multiscale and multimodel simulation of Bloch-point dynamics.* Physical Review B, 2014. **89**(13): p. 134403.
18. Hertel, R., et al., *Ultrafast Nanomagnetic Toggle Switching of Vortex Cores.* Physical Review Letters, 2007. **98**(11): p. 117201.
19. Hertel, R. and C.M. Schneider, *Exchange Explosions: Magnetization Dynamics during Vortex-Antivortex Annihilation.* Physical Review Letters, 2006. **97**(17): p. 177202.
20. Thiaville, A., et al., *Micromagnetic study of Bloch-point-mediated vortex core reversal.* Physical Review B, 2003. **67**(9): p. 094410.
21. Kardjilov, N., et al., *Three-dimensional imaging of magnetic fields with polarized neutrons.* Nature Physics, 2008. **4**(5): p. 399-403.
22. Manke, I., et al., *Three-dimensional imaging of magnetic domains.* Nat Commun, 2010. **1**: p. 125.
23. Donnelly, C., et al., *High-resolution hard x-ray magnetic imaging with dichroic ptychography.* Physical Review B, 2016. **94**(6): p. 064421.
24. Holler, M., et al., *X-ray ptychographic computed tomography at 16 nm isotropic 3D resolution.* Scientific Reports, 2014. **4**.

25. Phatak, C., M. Beleggia, and M. De Graef, *Vector field electron tomography of magnetic materials: Theoretical development.* Ultramicroscopy, 2008. **108**(6): p. 503-513.
26. Burzo, E., *Paramagnetic Behavior of Some Rare-Earth Cobalt Compounds.* Physical Review B, 1972. **6**(7): p. 2882-2887.
27. Chukazumi, S., in *Physics of Ferromagnetism*. 2009, OUP Oxford.
28. Stoehr, J. and H. Siegmann, *Magnetism: From fundamentals to Nanoscale Dynamics*. 2006: Springer.
29. Scagnoli, V., et al., *Linear polarization scans for resonant X-ray diffraction with a double-phase-plate configuration.* Journal of Synchrotron Radiation, 2009. **16**: p. 778-787.
30. van Heel, M. and M. Schatz, *Fourier shell correlation threshold criteria.* Journal of Structural Biology, 2005. **151**(3): p. 250-262.
31. Schäfer, R., *Domains in 'extremely' soft magnetic materials.* Journal of Magnetism and Magnetic Materials, 2000. **215–216**: p. 652-663.
32. Yu-Tung, C., et al., *Full-field hard x-ray microscopy below 30 nm: a challenging nanofabrication achievement.* Nanotechnology, 2008. **19**(39): p. 395302.
33. Cloetens, P., et al., *Holotomography: Quantitative phase tomography with micrometer resolution using hard synchrotron radiation x rays.* Applied Physics Letters, 1999. **75**(19): p. 2912-2914.
34. Robisch, A.L., et al., *Holographic imaging with a hard x-ray nanoprobe: ptychographic versus conventional phase retrieval.* Optics Letters, 2016. **41**(23): p. 5519-5522.
35. Eriksson, M., J.F. van der Veen, and C. Quitmann, *Diffraction-limited storage rings - a window to the science of tomorrow.* Journal of Synchrotron Radiation, 2014. **21**: p. 837-842.
36. Thibault, P., M. Guizar-Sicairos, and A. Menzel, *Coherent imaging at the diffraction limit.* Journal of Synchrotron Radiation, 2014. **21**: p. 1011-1018.
37. Rodenburg, J.M., et al., *Hard-x-ray lensless imaging of extended objects.* Physical Review Letters, 2007. **98**(3): p. 4.
38. Thibault, P., et al., *High-resolution scanning x-ray diffraction microscopy.* Science, 2008. **321**(5887): p. 379-382.
39. Tripathi, A., et al., *Dichroic coherent diffractive imaging.* Proceedings of the National Academy of Sciences of the United States of America, 2011. **108**(33): p. 13393-13398.
40. Giles, C., et al., *Energy-Dispersive Phase Plate for Magnetic Circular-Dichroism Experiments in the X-ray Range.* Journal of Applied Crystallography, 1994. **27**: p. 232-240.
41. Dierolf, M., et al., *Ptychographic X-ray computed tomography at the nanoscale.* Nature, 2010. **467**(7314): p. 436-U82.
42. Henrich, B., et al., *PILATUS: A single photon counting pixel detector for X-ray applications.* Nuclear Instruments & Methods in Physics Research Section a-Accelerators Spectrometers Detectors and Associated Equipment, 2009. **607**(1): p. 247-249.
43. Kraft, P., et al., *Characterization and Calibration of PILATUS Detectors.* Ieee Transactions on Nuclear Science, 2009. **56**(3): p. 758-764.
44. Guizar-Sicairos, M. and J.R. Fienup, *Phase retrieval with transverse translation diversity: a nonlinear optimization approach.* Optics Express, 2008. **16**(10): p. 7264-7278.
45. Thibault, P. and M. Guizar-Sicairos, *Maximum-likelihood refinement for coherent diffractive imaging.* New Journal of Physics, 2012. **14**: p. 063004.
46. Bouchenoire, L., et al., *Performance of phase plates on the XMaS beamline at the ESRF.* Journal of Synchrotron Radiation, 2003. **10**(2): p. 172-176.
47. Guizar-Sicairos, M., S.T. Thurman, and J.R. Fienup, *Efficient subpixel image registration algorithms.* Optics Letters, 2008. **33**(2): p. 156-158.
48. Guizar-Sicairos, M., et al., *High-throughput ptychography using Eiger: scanning X-ray nano-imaging of extended regions.* Optics Express, 2014. **22**(12): p. 14859-14870.
49. Guizar-Sicairos, M., et al., *Phase tomography from x-ray coherent diffractive imaging projections.* Optics Express, 2011. **19**(22): p. 21345-21357.

50. Guizar-Sicairos, M., et al., *Quantitative interior x-ray nanotomography by a hybrid imaging technique.* Optica, 2015. **2**(3): p. 259-266.
51. Hannon, J.P., et al., *X-Ray Resonance Exchange Scattering.* Physical Review Letters, 1988. **61**(10): p. 1245-1248.
52. Howells, M.R., et al., *An assessment of the resolution limitation due to radiation-damage in x-ray diffraction microscopy.* J Electron Spectros Relat Phenomena, 2009. **170**(1-3): p. 4-12.